The Astrophysical Journal Letters, 990:L40 (10pp), 2025 September 10 https://doi.org/10.3847/2041-8213/adfadb

High Resolution ALMA Data of the Fomalhaut Debris Disk Confirms Apsidal Width Variation

Jay S. Chittidi[1,2], Meredith A. MacGregor[1], Joshua Bennett Lovell[3], Gaspard Duchene[4,5], Mark Wyatt[6], Olja Panic[7], Paul Kalas[4,8,9], Margaret Pan[3], A. Meredith Hughes[10], David J. Wilner[3], Grant M. Kennedy[11], Luca Matrà[12], Michael P. Fitzgerald[13], and Kate Y. L. Su[14]

[1] Department of Physics & Astronomy, John Hopkins University, 3400 North Charles Street, Baltimore, MD 21218, USA
[2] Department of Astrophysical and Planetary Sciences, University of Colorado, 2000 Colorado Avenue, Boulder, CO 80309, USA
[3] Center for Astrophysics, Harvard & Smithsonian, 60 Garden Street, Cambridge, MA 02138-1516, USA
[4] Astronomy Department, University of California, Berkeley, CA 94720-3411, USA
[5] Université Grenoble Alpes/CNRS, Institut de Planétologie et d'Astrophysique de Grenoble, 38000 Grenoble, France
[6] Institute of Astronomy, University of Cambridge, Madingley Road, Cambridge CB3 0HA, UK
[7] School of Physics and Astronomy, University of Leeds, Leeds LS2 9JT, UK
[8] Institute of Astrophysics, FORTH, GR-71110 Heraklion, Greece
[9] Carl Sagan Center, SETI Institute, 189 Bernardo Avenue, Mountain View, CA 94043, USA
[10] Department of Astronomy, Van Vleck Observatory, Wesleyan University, Middletown, CT 06459, USA
[11] Department of Physics and Centre for Exoplanets and Habitability, University of Warwick, Gibbet Hill Road, Coventry CV 4 7AL, UK
[12] School of Physics, Trinity College Dublin, The University of Dublin, College Green, Dublin 2, Ireland
[13] Department of Physics and Astronomy, UCLA, Los Angeles, CA 90095, USA
[14] Space Science Institute, 4750 Walnut Street, Suite 205, Boulder, CO 80301, USA
Received 2025 March 19; revised 2025 July 10; accepted 2025 July 11; published 2025 September 4

Abstract

We present long-baseline observations of the Fomalhaut outer debris disk at 223 GHz (1.3 mm) from Atacama Large Millimeter/submillimeter Array (ALMA) Cycle 5, which we use along with archival short-baseline observations to produce a 0.″57 resolution mosaic of the disk at a sensitivity of 7 μJy bm^{-1}. We use radial profiles to measure the disk at the ansae and find that the southeast (SE) side of the disk is 4 au wider than the northwest (NW) side as observed by ALMA. We also find that the peak brightness of the NW ansa is 21% ± 1% brighter than the SE ansa. We perform Markov Chain Monte Carlo fits of the ALMA visibilities using two analytical, eccentric disk models. Our results suggest that the model including a dispersion parameter for the proper eccentricity (σ_{e_p}), which accounts for additional scatter in the eccentricity of individual orbits, is preferred over the model without one. Such a model implies that self-gravitation, particle collisions, and close-packing could play a role in shaping the overall structure of the Fomalhaut disk, as is seen in eccentric planetary rings. Crucially, neither model can reproduce the brightness or width asymmetry near the NW ansa. No emission from the intermediate belt is detected, allowing us to place a 3σ upper limit of 396 μJy at 1.3 mm. We also discover a spectral line in archival Cycle 3 data centered at $\nu_{\rm obs} \approx 230.25$ GHz at the location of the "Great Dust Cloud," whose redshift from the expected CO line for Fomalhaut confirms the source is a background galaxy.

Unified Astronomy Thesaurus concepts: Debris disks (363); Planet formation (1241)

1. Introduction

Fomalhaut is a nearby (∼7.7 pc, F. van Leeuwen 2007) A3V star with an estimated age of 440 Myr (E. E. Mamajek 2012). Observations from the Infrared Astronomical Satellite decades ago revealed a strong infrared excess indicative of circumstellar dust, making the system an exciting site to study planetary dynamics and disk evolution (D. E. Backman & F. Paresce 1993). Low-resolution imaging observations with the Submillimetre Common-User Bolometer Array at the James Clerk Maxwell Telescope revealed asymmetric emission from the debris disk at the southern ansa (W. S. Holland et al. 1998). M. C. Wyatt et al. (1999) noted that this could be evidence of an eccentric disk sculpted by an eccentric, hidden planet, resulting in increased thermal emission near the disk's pericenter (presumably the southern ansa). Spitzer observations presented in K. R. Stapelfeldt et al. (2004) showed further evidence of this "pericenter glow." Hubble Space Telescope imaging resolved the outer cold belt (∼140 au, P. Kalas et al. 2005) and later the appearance of what was initially thought to be a planet but is now thought to be an expanding dust cloud just interior to the disk (P. Kalas et al. 2008; S. J. Kenyon et al. 2014; S. M. Lawler et al. 2015; A. Gáspár & G. Rieke 2020). The optical imaging with Hubble revealed that the disk was eccentric, and both HST and far-infrared imaging with Herschel observed pericenter glow (B. Acke et al. 2012). Notably, longer-wavelength imaging using facilities such as the Atacama Large Millimeter/submillimeter Array (ALMA) has shown a pronounced brightness enhancement at the northern ansa, analogously called "apocenter glow" (M. A. MacGregor et al. 2017). M. Pan et al. (2016) argue that apocenter glow is due to a surface density enhancement from particles traveling slowest (and hence spending more time) at apocenter, while recent theoretical work done by E. M. Lynch & J. B. Lovell (2022) argue that such features also depend on the eccentricity profile of the disk. JWST MIRI imaging presented in A. Gáspár et al. (2023) further revealed the presence of an inner disk of warm

grains, a previously undiscovered intermediate belt (IB) at ∼90 au just interior to the main belt, and an extended halo of dust from the outer belt also present in HST imaging (P. Kalas et al. 2013). Recently, M. Sommer et al. (2025) presented an analysis that demonstrated that the emission from the inner and possibly IBs could be the natural consequences of Poynting–Robertson drag acting on smaller dust grains from the outer belt. Later, JWST NIRCAM imaging presented in M. Ygouf et al. (2024) placed constraints on planet masses $\leqslant M_J$ beyond about 8 au. They found one possible new candidate source ("S7") that future observations will need to search for to verify if it is associated with Fomalhaut. The presence of multiple eccentric debris belts and their multiwavelength brightness distributions provides an exciting but complex system to study the processes that drive the evolution of planetary systems.

ALMA has revolutionized our understanding of planetesimal disks making many dozens of detections of Kuiper Belt analogs including the Fomalhaut outer belt itself (A. G. Sepulveda et al. 2019; S. Marino 2019, 2022). A. C. Boley et al. (2012) observed the disk in ALMA Cycle 0 and found that the disk's edges were sharper than expectations for the system, and appeared consistent with sculpting from an inner and possibly outer planetary mass companion. M. A. MacGregor et al. (2017) used ALMA to produce a mosaic map of the disk in Band 6 at 223 GHz, providing high resolution (natural weight beam size of $1\farcs56 \times 1\farcs15$) and sensitivity (rms of 14 μJy beam^{-1}) in the submillimeter regime for the disk, and showed that a model which treats the complex eccentricity as the vector sum with a proper and forced component with independent phase parameters was a good match to the observations. G. M. Kennedy (2020) found that those same observations showed evidence that the northwest (NW) ansa of the disk was narrower than the southeast (SE) ansa by about 4 au (measured from the full width at half-maximum; FWHM), and demonstrated that a modified version of the complex eccentricity model that included a dispersion in the forced eccentricity could allow for a narrower NW ansa (proximate to the disk apocenter).

Here, we present new ALMA observations that reveal the Fomalhaut debris disk at unprecedented resolution at millimeter wavelengths allowing us to more accurately constrain the geometry of the outer belt. This letter is organized as follows. In Section 2, we discuss the ALMA data sets, their processing, and our method to correct for the proper motion between the three epochs. In Section 3, we present continuum images of the aligned data sets and discuss the `CLEAN` parameters that were used to produce them. We then present Markov Chain Monte Carlo (MCMC) fit results for two eccentric disk models in Section 4. We measure and discuss the widths of the disk at the ansae using radial profiles of the disk images that have been regridded to R–θ space in Section 5.1. Specifically, we find that while we can still model the bulk parameters of Fomalhaut's eccentric ring, our models do not provide a good physical interpretation for the disk's asymmetries identified in the higher-resolution data (i.e., the width and brightness differences at the ansae). We also present the detection of a spectral line coincident with the "Great Dust Cloud" (GDC) source discussed in A. Gáspár et al. (2023) and G. M. Kennedy et al. (2023), which corroborates its nature as a background galaxy rather than an object associated with the Fomalhaut system. Finally, we discuss our interpretation in the context of alternative descriptions of this system, such as those with differences in their radial profile parameterizations and orbital eccentricity distributions of orbital eccentricities, including that of J. B. Lovell et al. (2025) analyzing these same observations.

Table 1
ALMA Observations from Project 2017.1.01043.S

Date	Antennas	Baselines (m)	PWV (mm)	Obs. Time (minutes)
2018 Sep 8	45	15.1–783.5	1.3	73.1
	45	15.1–783.5	1.2	72.7
2018 Sep 17	45	15.1–1245.6	0.4	78.4
2018 Sep 23	48	15.1–1397.8	0.5	73.1
2018 Sep 26	47	15.1–1397.8	0.8	73.7

2. Data

Three epochs of ALMA data in Band 6 were obtained from the archive: a high-resolution pointing on the central star observed in Cycle 2 (J. A. White et al. 2017, ID#2013.1.00486.S), a seven-pointing mosaic from Cycle 3 (M. A. MacGregor et al. 2017, ID#2015.1.00966.S), and two high-resolution pointings at the disk apses from Cycle 5 (ID#2017.1.01043.S). The Cycle 5 observations are summarized in Table 1. The observations from Cycle 2 were calibrated using ALMA pipeline version 4.3.1, the Cycle 3 data were processed with 4.5.3, and the Cycle 5 data with version 5.1.1-5, all of which are the pipeline versions recommended by ALMA support for each respective data set. The flux calibration and data weights were inspected across the three data sets and were found to be consistent across the three epochs, given their respective baseline coverage, and so no further changes were made to either product. We used two versions of `CASA` for this work: version 6.5.1-23 was used for all data manipulation tasks such as averaging and visibility model subtraction, while version 6.6.0-20 was used exclusively for imaging due to relevant updates to `tclean`.

The data were then concatenated into a single `CASA` measurement set. To reduce the data volume, the measurement set was averaged down to 8 channels for the three continuum spectral windows and 128 channels for the spectral window centered on the 230.538 GHz CO line. We then time averaged the data to 30 s intervals.

Self-calibration was attempted to correct for phase offsets introduced from the star's proper motion (328.95, −164.67 mas yr^{-1}, comparable to the net beam size across the three epochs, F. van Leeuwen 2007), but was unsuccessful due to low signal-to-noise ratio. Instead, we used the `CASA` implementation of `uvmodelfit` (I. Martí-Vidal et al. 2014) to fit for the position of the star for each unique observation and pointing (a total of 52 fits). We then used the last observation from the Cycle 3 data as the reference position of the star, $\alpha = 22^{\rm h}57^{\rm m}39.450801$ and $\delta = -29°37'22\farcs69400$, and used the `fixplanets` and `fixvis` functions to manually correct the phase center and UVW baseline positions to the reference stellar position. To validate the proper motion correction, we imaged each of the 52 separate pointings/observations and analyzed the stellar position in the images for each set of pointings. We found that the stellar centroid position was precise to two pixels (∼0.″1, or about 1/5 of the synthesized beam of the image in Section 3). The scatter is dominated by the star coinciding with the first null in the

primary beam for the NW ansa pointing from the seven-pointing Cycle 3 data. The resulting measurement set is proper motion corrected for any emission comoving with the star and debris disk, but with smeared emission for background sources.

3. Imaging

The data were imaged together using the multifrequency synthesis task in `tclean` implemented in `CASA` v.6.6.0-20 in three ways: first we highlight just the NW and SE ansae pointings from only the Cycle 5 data, then we evaluate those same two pointings but with the shorter-baseline Cycle 3 data to highlight the improvement to the total flux, and finally we mosaic all of the available data in Band 6 to produce a single image. We opted to use the `multiscale` deconvolution method with the parameter `scales=[0,10,20]`, which allows for Gaussian sources in the `CLEAN` model map equal to the number of pixels specified by `scales` (0 is equivalent to typical `CLEAN` point source). We found that this resulted in a `CLEAN` model that looked more like a continuous, resolved disk rather than a collection of point sources as produced with the `hogbom` algorithm. Since the mosaics were constructed with uneven sensitivity across the pointings, and the disk extends across any individual pointing, all of the images presented here are primary-beam corrected. The image pixel scale was set so that the synthesized beam major axis covered approximately 10 pixels given the selected data for each image, and then the choice of `scales` was determined experimentally so that the largest scale was smaller than the apparent width of the disk. In addition, we used an elliptical `CLEAN` mask that encompassed the outer disk and star with parameters: $\alpha = 22^{\rm h}57^{\rm m}39.443347$, $\delta = -29°37'21\farcs12931$, $a = 25''$, $b = 12\farcs5$, and $\theta = 338°$. For the image of just the Cycle 5 data, we imaged the data to the 5% gain level to include the strongly-detected star, but used a primary-beam mask at the 30% gain level in lieu of the elliptical mask discussed above to avoid creating anomalously bright `CLEAN` sources at the edge of the primary beam. The combined Cycle 3 and 5 image, as well as the full mosaic were imaged to the 20% gain level. All images were `CLEAN`ed to 3× the rms noise level. We present naturally-weighted images in this letter in Figure 1. Briggs-weighted images are presented and analyzed in J. B. Lovell et al. (2025).

In Figure 1(a), we show the image of the Cycle 5 data, while in Figure 1(b) we show the combined Cycle 3 and Cycle 5 data. The rms noise near the phase centers is about 7 μJy, and the naturally-weighted beam sizes are $0\farcs50 \times 0\farcs39$ and $0\farcs57 \times 0\farcs44$, respectively. In Figure 1(c), we present the mosaic image of all of the available data. The synthesized beam size is $1\farcs09 \times 0\farcs81$ and the rms noise near the pointing centers is also 7 μJy. The different resolutions between the Cycle 2 and Cycle 5 data and the lack of high-resolution observations for the four "intermediate" pointings adjacent to the disk minor axis result in image artifacts that increase the rms noise near the star. In addition, the inconsistent resolution effectively results in a restoring beam size that is larger than the naturally-weighted beam size for the data at the disk ansae (Figure 1(b)), and so in the analysis that follows we consider both the full and partial mosaics depending on our use case. The disk modeling in Section 4 bypasses the nonlinearity inherent to `CLEAN` and the above artifacts altogether by directly comparing the data and model visibilities.

3.1. Image Analysis

In order to analyze azimuthal variations in the width of the disk, we deproject the disk image from Figure 1(b) (which has a smaller beam size than the full mosaic) using the best-fit inclination and position angle from the MCMC results presented later in Table 2, $i = 66\fdg5$ and PA $= 335\fdg84$. We then resample the image onto a grid of the circumstellar radius and azimuthal angle by averaging the flux of pixels corresponding to the same dR–$d\theta$ bin, presented in Figure 2(a). The angular coordinates are measured relative to the disk's position angle (i.e., the sky plane), so 0° and 360° correspond to $335\fdg84$ on the sky. In this view, the true pericenter and apocenter appear to occur at ≈45°, consistent with the results presented later for the ω_f parameter from the MCMC fits (though we note that the apparent apsides from these plots alone are obscured by both the disk scale height and change in resolution due to the beam position angle). The projection leads to increased artifacts at the disk minor axes, though this region is masked by our choice of the primary beam limit in the two-pointing mosaic.

We then use the deprojected map to create 1D radial profiles using a 10° wedge centered at the disk ansae (0° and 180° along the x-axis) in Figure 2(e). The 3σ uncertainty in the ALMA data profiles are plotted by using the 7 μJy beam^{-1} measured in the image and as a function of number of binned pixels relative to the number of pixels in the beam area: $\sigma_{\rm profile} = 7\ \mu{\rm Jy}\sqrt{N_{\rm pix/beam}/N_{\rm pix/bin}}$. We compare the peak-to-peak brightness ratio between the radial profiles and measure a $21\% \pm 1\%$ brightness enhancement at the NW ansa, a larger difference than reported in M. A. MacGregor et al. (2017). This likely results from the low resolution of the 2017 observations, which do not fully resolve the disk's width. Considering just the SE ansa of the disk, the peak brightness is 0.21 ± 0.02 and 0.25 ± 0.03 mJy arcsec^{-2} in the 2017 data and the new data presented here (Figure 1(a)), respectively, consistent within the mutual uncertainties. The difference in peak brightness is more noticeable at the NW ansa where the peaks are 0.23 ± 0.02 and 0.30 ± 0.03 mJy arcsec^{-2}, respectively. However, the NW ansa is where the resolution difference between the two data sets is most significant given the narrow disk width. We compute the integrated flux to be 0.23 ± 0.02 mJy and 0.27 ± 0.03 mJy, respectively, to account for this resolution difference and note that these values also overlap within the mutual uncertainties.

We compute the width of the disk at each ansa by measuring the FWHM of the radial profiles. The FWHM is 16 au for the SE ansa profile, and 12 au for NW ansa profile, resulting in a width difference of 4 au. The widths are denoted as the highlighted regions in Figure 2(e). G. M. Kennedy (2020) also measured a 4 au FWHM width difference, although the respective ansae also each appeared 4 au wider at lower resolution.

The radial profiles analyzed here also have a complex shape. We identify the presence of "shoulders" of emission located at about 15–20 au interior and exterior to the emission peaks (see the colored arrows in Figure 2(e)). The inner edge of the apocenter ansa radial profile is also sharper than the outer edge or the pericenter ansa profile. We assess how these extended features influence the profile shape by measuring the full width at 20% maximum. At this lower flux threshold, the SE ansa width is 29 au and the NW ansa width is 21 au, or twice the width difference as before. This suggests that these low surface brightness features are significant. In the

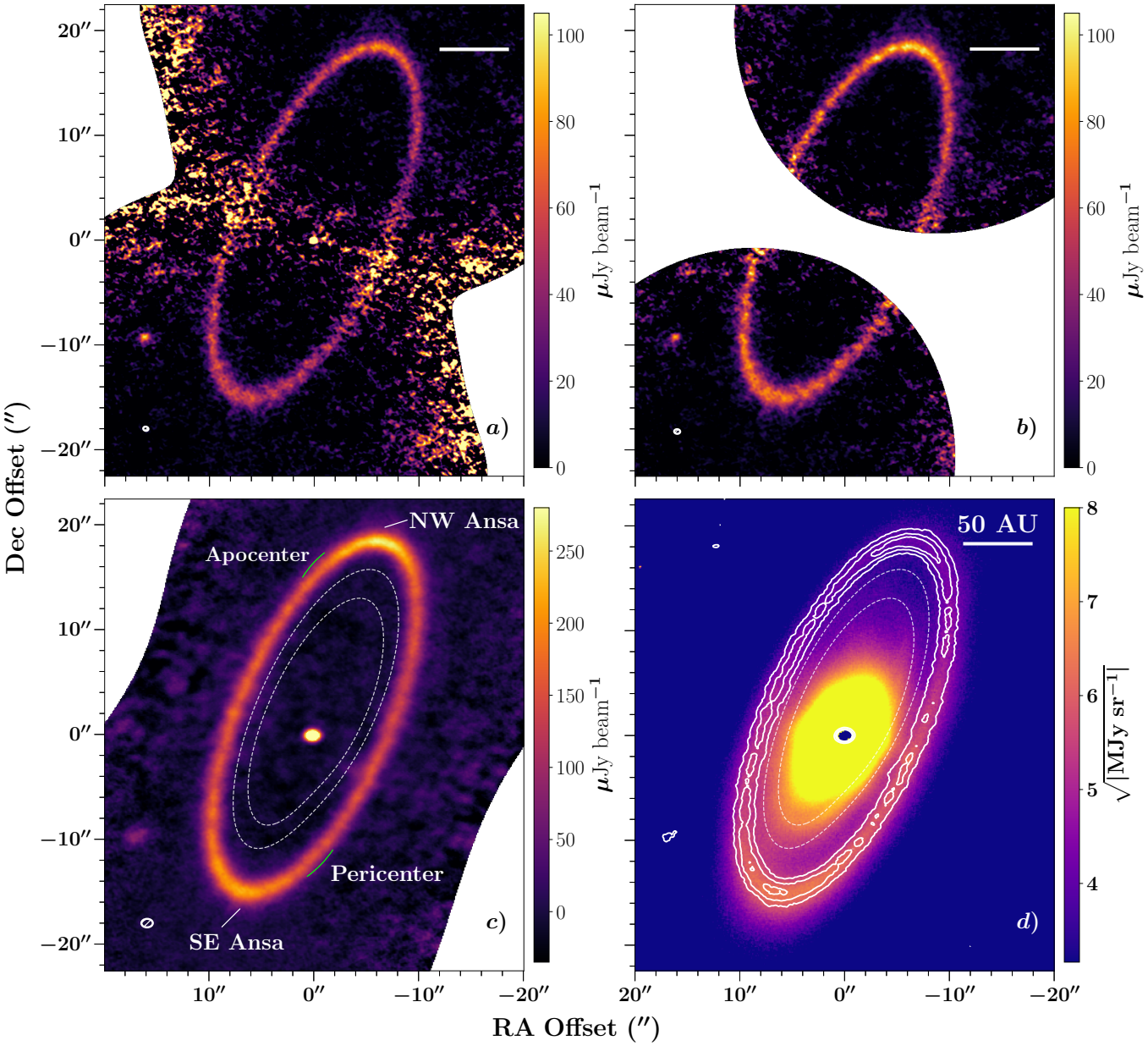

Figure 1. Top left: A mosaic of the Cycle 5 (C5) long-baseline data. The data were imaged to the 5% gain level to highlight the detection of the star, which sits at the edge of the primary beam between the NW and SE ansae pointings. The naturally-weighted beam size is 0.″50 × 0.″39 (indicated by the ellipse in the lower left corner of each panel) and the rms noise near the pointing centers is 7 μJy bm^{-1}. The axes are the stellocentric offset in arcseconds and the image is north-aligned. Top right: A mosaic of the NW and SE ansae pointings using the coaligned shorter-baseline Cycle 3 (C3) data as well as the longer baseline C5 data. The naturally-weighted beam size is slightly larger, 0.″57 × 0.″44, and the rms is also 7 μJy bm^{-1}. Bottom left: A mosaic of all seven pointings of ALMA Band 6 observations from C2, C3, and C5. The naturally-weighted beam size is 1.″09 × 0.″81 and the rms noise near the pointing centers at the ansae is 7 μJy bm^{-1}, but decreases to 12 μJy bm^{-1} toward the IB (denoted by the dashed white curves, see Section 5.2). The lack of long-baseline observations at the intermediate pointings leads to a beam size that is larger than the naturally-weighted beam corresponding to just the NW and SE ansae data, as in the top right. Bottom right: JWST 25.5 μm image from A. Gáspár et al. (2023) with overlaid contours from the bottom right ALMA mosaic corresponding to the 10σ, 20σ, and 30σ flux levels. This image has been scaled to highlight the intermediate and inner disks, and the positions of the contours have been corrected for the proper motion between the two imaged epochs. The fainter dashed curves denote the IB boundaries as in the bottom left.

subsequent modeling section, we consider two eccentric disk models. Of key concern is whether either of these models are able to reproduce the 21% brightness enhancement at apocenter and the approximately 4 au difference in width identified in the data.

4. Eccentric Disk Models

The underlying orbital parameters that describe the surface brightness distribution are modeled using a particle-based approach that was investigated in M. A. MacGregor et al. (2017) and G. M. Kennedy (2020) (and more recently for the HD 53143 disk in M. A. MacGregor et al. 2022). We consider two disk models with complex forced and proper eccentricities, e_f and e_p. The first model most closely mirrors the model initially studied in M. A. MacGregor et al. (2017), while the second model includes an additional free parameter for a Gaussian dispersion in the proper eccentricity, which G. M. Kennedy (2020) demonstrated could allow for a narrower apocenter than pericenter.

Table 2
Eccentric Disk Model Posteriors

Parameter	Model Without σ_{e_p}	Model With σ_{e_p}
a [au]	$139.48^{+0.39}_{-0.39}$	$139.48^{+0.43}_{-0.42}$
Δa [au]	$10.88^{+2.33}_{-2.95}$	$6.66^{+2.06}_{-2.62}$
$F_{\rm disk}$ [mJy]	$21.95^{+0.54}_{-0.53}$	$22.99^{+0.72}_{-0.68}$
$F_{\rm star}$ [mJy]	$0.77^{+0.01}_{-0.01}$	...
i [°]	$66.50^{+0.11}_{-0.10}$	$66.50^{+0.11}_{-0.11}$
PA [°]	$335.84^{+0.11}_{-0.12}$	$335.84^{+0.11}_{-0.11}$
e_f	$0.15^{+0.01}_{-0.01}$	$0.14^{+0.01}_{-0.01}$
e_p	$0.03^{+0.01}_{-0.01}$	$0.02^{+0.01}_{-0.01}$
σ_{e_p}	...	$0.06^{+0.01}_{-0.01}$
ω_f [°]	$45.94^{+1.38}_{-1.51}$	$41.89^{+2.94}_{-4.18}$
R.A.$_{\rm off}$ [″]	$0.08^{+0.01}_{-0.01}$	$0.08^{+0.01}_{-0.01}$
Decl.$_{\rm off}$ [″]	$-0.05^{+0.01}_{-0.01}$	$-0.05^{+0.01}_{-0.01}$
h	$0.01^{+0.01}_{-0.01}$	$0.02^{+0.01}_{-0.01}$
BIC	27815115	27811668

For both models, the mean longitude, l, and argument of periastron, ω_p, of orbiting particles are drawn from a uniform distribution between 0 and 2π. Then, the particles populate the complex eccentricity plane defined by three free parameters: the forced eccentricity, e_f, the forced argument of periastron, ω_f, and the proper eccentricity, e_p. For the second model, the proper eccentricity is drawn from a normal distribution whose mean is e_p and standard deviation is σ_{e_p}. To avoid nonphysical parameters, we take the absolute value of e_p so $e_p > 0$, and redraw particles from the distribution when $e_p > 1$. We then solve Kepler's equation for the true anomaly, f, with the `kepler` code (D. Foreman-Mackey et al. 2021).

Next, the semimajor axis of each particle is drawn from a uniform distribution defined between $a - \Delta a/2$ and $a + \Delta a/2$, where a and Δa are free parameters. Then, the radial position of each particle is solved by the equation

$$r = \frac{a(1 - e^2)}{1 + e\cos(f)}, \tag{1}$$

where f is the true anomaly.

The particles are given a height, z, about the disk midplane and are drawn from an exponential distribution defined by a single free parameter scale height, h, such that $z = h/r$. We also account for the disk's geometry, fitting for an inclination, i, and position angle, PA, defined north to east. R.A. and decl. offsets (positive in the north and east directions, respectively) account for any global pointing offset.

To create an image, we bin the particles onto a 2D spatial grid (histogram) whose values are then scaled by $r^{-0.5}$ in order to simulate a temperature profile. The total disk flux is normalized such that $F_{\rm belt} = \int I_\nu d\Omega$ and a point source representing the star is added with flux $F_{\rm star}$. To simplify comparison, we ensure that both models have 12 free parameters by fixing the stellar flux to $F_{\rm star} = 0.735$ mJy for the second model with $\sigma_{e_p} > 0$. This lower value for the stellar flux was based on an early fit to the data, but this is independent of the parameters for the disk and should not impact the best-fit parameters. However, when we compute the Bayesian information criterion (BIC) using the median parameters from the `emcee` posteriors, we use the stellar flux from the first model for an even comparison.

G. M. Kennedy (2020) and J. B. Lovell & E. M. Lynch (2023) demonstrated that line density models such as the one considered here need a sufficient number of particles in order to reduce the shot-noise associated with the randomly-generated model and to effectively sample the surface density distribution under the beam. G. M. Kennedy (2020) used 10^7 particles to model the C3 data with a dispersion parameter, which we estimate resulted in a 0.2% model-induced error based on the shot-noise analysis presented in Figure A1 of J. B. Lovell & E. M. Lynch (2023). We use that same analysis to determine that we would need $\mathcal{O}(10^8)$ particles in order to achieve a similar level of shot-noise at the C5 resolution of 0.″5. We use `galario` (M. Tazzari et al. 2018) to sample the model images into visibilities to compare with the ALMA data. For each unique observation ID, spectral window, and field, the model image is offset to the correct relative pointing before comparing with the visibilities, and thus the net χ^2 for each model image is the sum of the χ^2 values for each unique offset. The parameter space is explored with the MCMC package `emcee` (D. Foreman-Mackey et al. 2013) using 80 walkers and 18,027 steps for the first model and 22,199 steps for the second model. We assess the models as having converged when the chains were run for at least 50 times the longest autocorrelation time for any of the parameters.

Analytic models like these have limitations and often fail to completely model complex systems. For example, the models we employ do not account for either density enhancements or disk broadening as a function of true anomaly. The Fomalhaut debris disk is likely dynamically influenced by at least one planet (e.g., A. C. Boley et al. 2012), so a complete model of the system would require use of N-body simulations. However, as noted above, this analytic model is computationally intensive. Attempting to fold an N-body simulation into this MCMC framework would take a prohibitive amount of computing resources. As a result, analytic models are extremely useful for understanding disk geometry and are widely used throughout the literature. Some N-body simulations are included in the companion paper to this letter (J. B. Lovell et al. 2025), and we defer more complicated modeling to future work.

4.1. Modeling Results

We present the median posterior parameters for both models in Table 2, and in Figure 3 we show the full-resolution (i.e., not `CLEAN`'ed or convolved with the synthesized beam) model images at the disk ansae. With these, we also present the residuals that have been repackaged into a `CASA` measurement set and imaged with the same `tclean` parameters as the full-mosaic presented in Figure 1(c).

The nominal disk semimajor axis, inclination, position angle, and scale height for both models are identical and are in good agreement with the analogous "uniform simple" and "uniform full" model fits presented in Table 1 of G. M. Kennedy (2020). The forced and proper eccentricities for the two models presented here are also in good agreement within their parameter uncertainties, but they do differ slightly from the results in G. M. Kennedy (2020). Here, we find that for the model without dispersion, the forced eccentricity is about 0.02 higher and the proper eccentricity is about 0.03 lower than the G. M. Kennedy (2020) results. For the model with dispersion, the results are more in agreement, but the σ_{e_p} parameter is about 0.03 lower in this work. This could be due

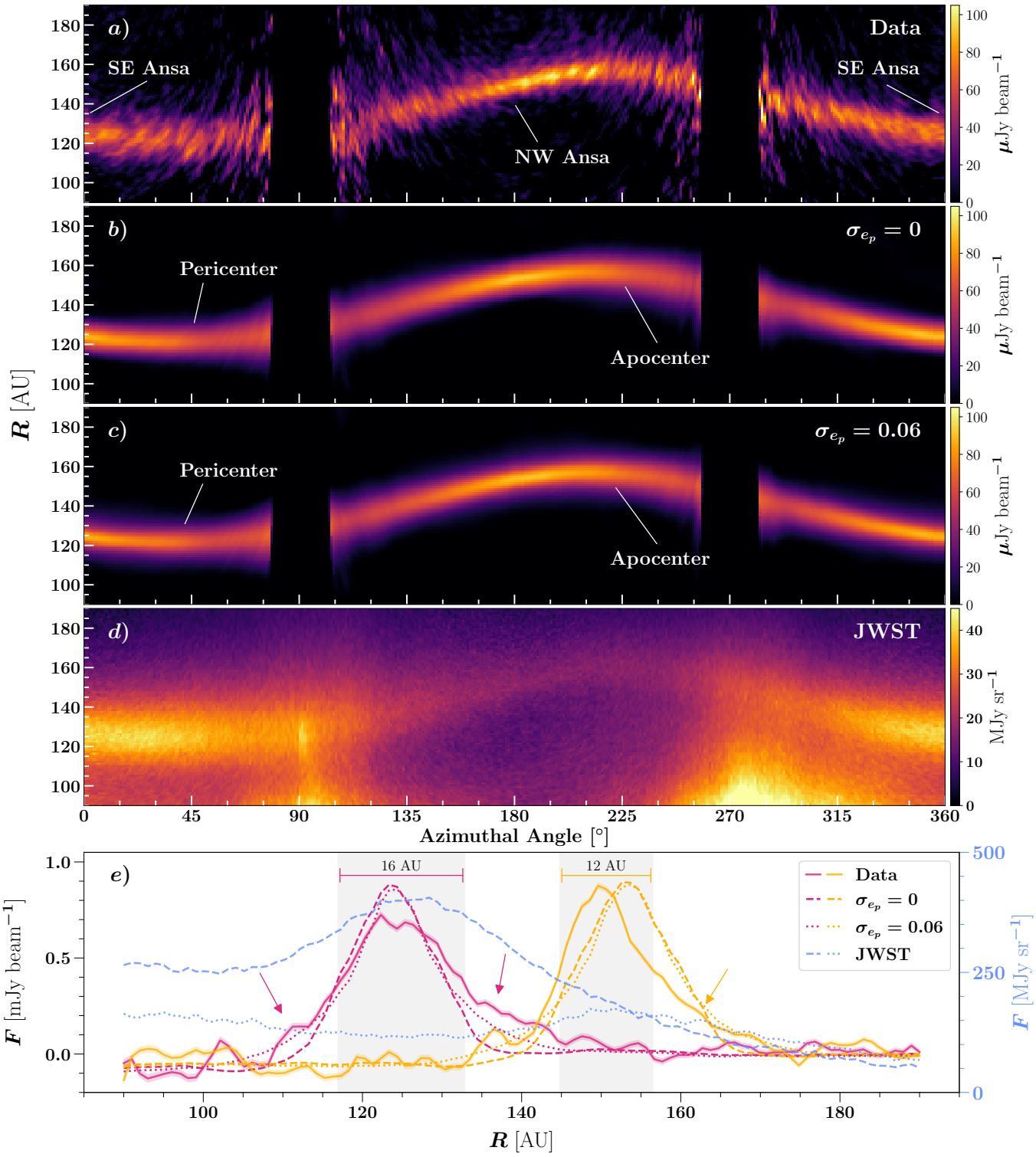

Figure 2. First row: A deprojected map of the circumstellar radius vs. azimuthal angle of the Fomalhaut outer disk produced using the mosaic in Figure 1(b). The angular coordinates are with respect to the disk position angle of 335.°84. Second row: A radius vs. azimuth map for the best-fit model without a dispersion in eccentricity, after imaging with CASA. Third row: Same as the second, but for the best-fit model with a dispersion in eccentricity. Fourth row: A radius vs. azimuth map of the 25.5 μm JWST image of the disk. Unlike the ALMA images, the NW ansa is significantly dimmer than the SE ansa. Fifth row: Radial profiles produced using 10° radial cuts centered at 0° (SE ansa near apocenter, red) and 180° (NW ansa near apocenter, yellow) from the above maps. For the ALMA data, the 21% ± 1% brightness asymmetry between the ansae is strongly apparent. The labeled shaded regions are the measured FWHM of the data. "Shoulders" of emission at 20 au interior and exterior to the peak flux in the SE ansa profile and exterior to NW ansa profile are denoted by the colored arrows. The radius of peak emission differ between the data and the models, which is discussed in the text.

to a combination of the choice of the uniform distribution of semimajor axes and the "shoulders." As seen in Figure 2(e), the peak emissions for both models near the apocenter side of the disk occur about 4 au further out than the data, toward the exterior "shoulder." The eccentricity parameters and choice of distribution could both affect where these peaks occur, and

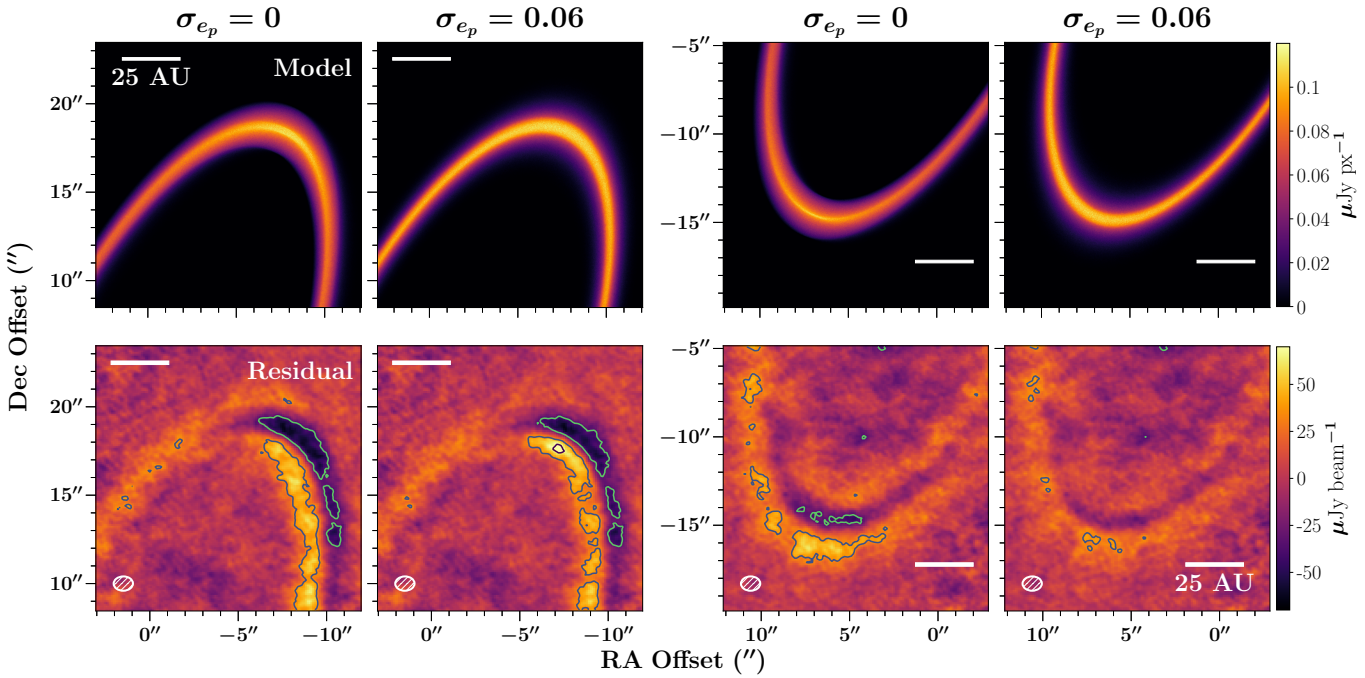

Figure 3. Top row: Apocenter and pericenter plots of the best-fit eccentric disk models without (first column) and with (second column) a free parameter describing a Gaussian dispersion in the proper eccentricity for the particles (see Table 2). These images are full-resolution, i.e., not convolved with the synthesized beam, in order to highlight the underlying differences in intensity. Bottom row: Residual between the data and model with contours highlighting -10σ, -5σ, 5σ, and 10σ noise level. These were imaged with `tclean` with the same parameters as in Figure 1(c). The ellipses indicate the size of the ALMA beam.

may explain why our results appear to differ from the literature and the data. Finally, the model with dispersion has a slightly lower argument of periastron that is comparable to the $41^\circ \pm 1^\circ$ constraint in G. M. Kennedy (2020). The difference in values between our two models does not appear to be statistically significant.

The most notable differences between the two models in this work are the disk's width and the total disk flux. The inclusion of the σ_{e_p} parameter was expected to reduce the disk's width such that the expression $\sqrt{(\Delta a)^2 + (a\sigma_{e_p})^2}$ should correspond to the disk's width without the dispersion parameter. Indeed, we find that the expression would yield an effective disk width of 10.70 au, in excellent agreement with the 10.88 au result for the model without the dispersion parameter. G. M. Kennedy (2020) reported a best-fit dispersion parameter of 0.09, higher than we find here, but this is likely related to the differences noted above. The model with dispersion has a total disk flux about 1 mJy brighter than the other model, though this difference is only at the 2σ significance level. This may be influenced by the "shoulders" observed in the radial profiles, since the model with dispersion has a wider profile that overlaps with these features while the model without the dispersion does not. M. A. MacGregor et al. (2017) reported a total disk flux of 24.7 ± 0.1 mJy, higher than either model here, either because the "shoulders" are unresolved in those observations or the inclusion of the long-baseline visibilities weigh down the total flux in the model fits in this work. Notably, neither model is able to reproduce the 21% flux difference between the ansae, instead producing roughly equal peaks.

We compute the BIC for our two models:

$$\mathtt{BIC} = k \ln(n_{\rm vis}) + \chi^2, \quad (2)$$

where k is the number of parameters (12 for both models) and $n_{\rm vis}$ is the total number of visibilities (real and imaginary, $>8.6 \times 10^6$). We include the BIC values in Table 2. The model with the lowest BIC is the preferred model, with differences of >10 indicating that the lower BIC is very-strongly preferred (R. E. Kass & A. E. Raftery 1995). We find that the model with σ_{e_p} is very-strongly preferred over the model without, in agreement with similar findings in G. M. Kennedy (2020).

5. Discussion

5.1. Variation of the Disk's Width

We generate additional radial maps for the two best-fit models (these are imaged with `CLEAN` using the same parameters as the two-pointing mosaic) and for the 25.5 μm JWST MIRI image using the same technique presented in Section 3.1. We compare radial profile cuts with the data in Figure 2(e). Rather critically, neither model investigated in this work seems to be able to reproduce the 21% brightness asymmetry or the 4 au width difference. The peak fluxes in the model profiles are nearly the same at each ansae and the measured FWHM appears to be 1 au wider at apocenter ansa—the complete opposite of the trend in the data. These measured widths are presented in Table 3.

The model radial profiles also elucidate the residuals present in Figure 3—these best-fit models have their peak emission occurring at slightly lower radii near pericenter and noticeably higher radii near apocenter compared to the data. This may be due to our choice of a uniform distribution for the disk particle semimajor axes. For example, a different prescription, such as a Gaussian, could alter where the peak brightness occurs. Some of the key parameters in the model fits are correlated (e.g., Δa and e_p in the $\sigma_{e_p} = 0$ model) or have non-Gaussian posterior distributions, and so the median parameter values selected for these models may not truly be the "best-fit" ones.

Table 3
Disk Ansae FWHM Measurements

Data Set	SE Ansa (au)	NW Ansa (au)
ALMA Band 6	16	12
$\sigma_{e_p} = 0$	12	13
$\sigma_{e_p} = 0.06$	11	12

One subtle detail in the model profiles that include a dispersion parameter is that the flux falls off more gently, resulting in wider low surface brightness features. This could at least partially explain the "shoulders" seen in the data, and may also be the reason this model is statistically preferred over the other one despite the fact that it cannot reproduce the brightness asymmetry or width difference. These "shoulders" appear slightly more distinct from the central peak of emission compared to the more smooth profile from the model, which may indicate that these are separate features. Edge sharpness can be used to constrain the properties of sculpting planets (e.g., T. D. Pearce et al. 2024). The fact that the preferred model has smoother edges could also imply that other dynamical processes might be involved in creating the eccentricity in the Fomalhaut disk, such as self-gravitation, particle collisions, and close-packing seen in planetary rings in the solar system (S. F. Dermott & C. D. Murray 1980). More detailed *N*-body simulations are needed to fully explore this. The exterior "shoulders" are also reminiscent of the halos detected in other debris disks, such as HD 32297, HD 61005, and q^1 Eri (M. A. MacGregor et al. 2018; J. B. Lovell et al. 2021), and targets from the ARKS survey (2025, in preparation, private communication). The differences in the shape of the radial profiles at the two ansae, including the exterior shoulders, appear consistent with an *N*-body simulation of an eccentric planet sculpting an exterior disk presented in Appendix B1 of T. D. Pearce et al. (2024), with a narrower apocenter and an exterior halo/shoulder, though the SE ansa profile of Fomalhaut appears more Gaussian than in that work. Higher-resolution observations in the future may be able to resolve just how distinct these features are.

Flux from the IB in the JWST MIRI image and the extended exterior halo complicate the width measurement, and so we instead cite a lower limit by measuring the width between where the flux radially outwards falls to the mean flux level about 25 au interior to the peak emission. In addition, the MIRI beam size is $\sim 1''$ or ~ 7.7 au, which is much larger than the ALMA beam. We place upper limits of 51 and 31 au on the SE and NW ansae in the JWST image, or a width difference of about 20 au between the ansae. However, if we instead compared where the flux level at the outer edge of the SE ansa is comparable to the flux beyond the dimmer NW ansa, the SE width could be as much as 20 au wider than estimated here. These estimates are better compared to the full width at 20% maximum measurements of 29 and 21 au at the SE and NW ansae from the ALMA data (Section 3.1).

Finally, we note that relatively high inclination of the disk degrades our ability to accurately measure the deprojected disk width away from the major axis (and is compounded by the increase in noise and artifacts in these same regions as discussed in Section 3).

5.2. Flux Constraints on the Intermediate Belt

We do not detect the IB revealed by JWST/MIRI (A. Gáspár et al. 2023) in the ALMA mosaic at 1.3 mm. In order to constrain the total flux for the IB at 1.3 mm, we estimate boundaries for the IB using parameters from A. Gáspár et al. (2023) and our forced and proper eccentricity model. A. Gáspár et al. (2023) note that the orbital boundaries of the IB are not well-defined due to the bright inner belt and the fainter NE ansa. They used ellipse fitting to estimate an inner boundary of $a = 83$ au, $e = 0.31$, and an outer boundary of $a = 104$ au, $e = 0.265$. They also found that the IB and inner belts had slightly varying inclinations and position angles, but for the sake of simplicity we ignore those differences here. Instead, we assume that the IB has a similar forced argument of pericenter as the outer belt, $\omega_f = 45°$, and trace out the orbits for the boundaries corresponding to all mean longitudes, $l = [0, 2\pi]$. These boundaries are plotted as white dashed lines in Figures 1(c) and (d).

The approximate rms noise and artifacts in the full-mosaic image (Figure 1(c)) increase away from the pointing center at the disk ansae, as discussed in Section 3. To measure this effect, we create an annulus region in `CASA` defined by the above boundaries, and use the `imstat` task to compute the rms, about 12 μJy bm^{-1}. We therefore put a 3σ upper limit on the peak flux of the IB at 1.33 mm of 36 μJy bm^{-1}. The area denoted by these approximate boundaries corresponds to $n_{\rm beams} = 121$. We then use the expression $F_{\rm lim} = (n_{\rm beams} \times {\rm rms})/\sqrt{n_{\rm beams}}$ to place a 3σ upper limit of 396 μJy on the IB flux at 1.33 mm. Using these same boundaries, we compute 56 mJy of flux in the JWST 25.5 μm image, although we note that this estimate is likely contaminated with flux from the inner belt.

M. Sommer et al. (2025) suggest the IB could be explained by P–R drag along with unmodeled features, like resonant trapping of small grains, without necessarily invoking a second, collisionally-active dust belt. Future SED modeling could use the upper limits these observations provide to clarify the nature of the IB.

5.3. Great Dust Cloud Detection

The spectral window corresponding to the C5 data centered on the $\nu_{21} = 230.538$ GHz CO 2–1 line of the residual measurement set (i.e., the best-fit σ_{e_p} continuum model was subtracted off) was imaged as a cube with `tclean`, and a Keplerian spatio-spectral mask was used in order to determine if CO emission from the exocometary debris could be detected as in L. Matrà et al. (2017). No emission was detected, but this result is consistent with the previous work given the higher resolution here.

However, upon reexamination of the disk model-subtracted C3 CO data, we discovered multiple consecutive channels of emission coincident with the position of the GDC object discussed in A. Gáspár et al. (2023) and G. M. Kennedy et al. (2023). The emission occurs between 230.1 and 230.4 GHz, corresponding to a linewidth of ≈ 300 km s^{-1}. Fomalhaut's systemic radial velocity is $v_r = 6.5$ km s^{-1} (G. A. Gontcharov 2006), which would imply that the emitting gas is moving with velocities >400 km s^{-1} if they were from the expected 230 GHz CO 2–1 line. Given the dynamics of debris disks and the relative size, velocity, and location of this feature, it seems implausible that it is connected to a feature in the Fomalhaut debris disk and is much more likely to be a

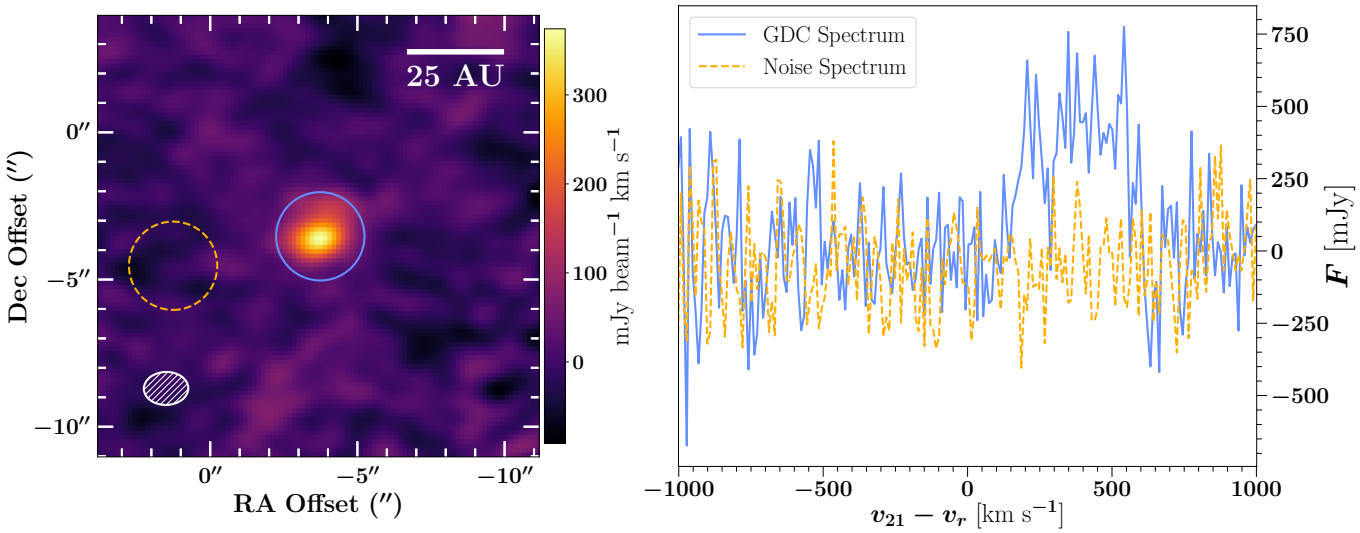

Figure 4. Left: A Moment-0 image of the GDC obtained by integrating between 230.1 and 230.4 GHz (173–563 km s^{-1} channels relative to the expected CO line) of the Cycle 3 residual measurement set (i.e., the best-fit disk continuum model has been subtracted off). The cyan circle denotes the area of the region used to extract the spectrum of the source, and the orange-dashed circle is denotes a region of equivalent size with characteristic noise. Right: The resulting extracted spectra of the background galaxy and noise region. The source emission is redshifted by >400 km s^{-1} from the expected Doppler-shifted transition of ^{12}CO $J = 2$–1 corresponding to Fomalhaut ($v_r = 6.5$ km s^{-1}, G. A. Gontcharov 2006), suggesting the source is unaffiliated with the system. The width of the emission is ≈300 km s^{-1}, consistent with velocity dispersion from rotating disk galaxies.

yet-unidentified spectral line emission from a background galaxy. In Figure 4, we produce a Moment-0 image of the spectral line from a primary-beam-corrected cube, and use two spatial filters to extract 1D source and noise spectra. No other sources appear in these channels above the noise level. The source was not detected in the C5 spectral window containing the ^{12}CO (2–1) transition, likely because this location corresponds to below the 20% gain level of the primary beam and thus may be lost in the noise.

M. Ygouf et al. (2024) fit the available photometry of the galaxy using template spectra of galaxies at $z =$ 0.80, 0.21, and 0.56 and concluded that the GDC was an ultraluminous infrared galaxy. On the assumption that this line emanates from CO (plausibly the brightest line and so most likely to be detected), we consider one possibility that the spectral line we identified is the ^{12}CO (3–2) transition at $\nu_{32} = 345.796$ GHz. Given that the observed central frequency of the line is at $\nu_{\rm obs} \approx 230.25$ GHz, we estimate a corresponding redshift of $z = 0.502$. It is unclear how uncertain the redshift estimates from the fits presented in M. Ygouf et al. (2024) are, but this could support the $z = 0.56$, NGC 6240-analog they proposed.

6. Conclusions

We used long-baseline observations from ALMA Cycle 5 and short-baseline observations from Cycle 3 to produce a 0.″57 (4.4 au) image of the Fomalhaut outer debris disk at a sensitivity of 7 μJy bm^{-1}.

1. We generated radial profiles of the new ALMA image and the 25.5 μm JWST/MIRI image from A. Gáspár et al. (2023) by regridding them to an R–θ grid. We then measured the FWHM of the radial profiles, and found that the SE side of the disk near pericenter is 4 au wider than at the NW side near apocenter with ALMA, and about 20 au wider with JWST. We also observed a 21% ± 1% brighter NW side compared to the SE side in the ALMA image from the peak brightness of the radial profiles.
2. We performed MCMC fits of two, particle-based disk models with proper and forced component eccentricities to the ALMA visibilities. Our BIC analysis suggests that the model that includes a σ_{e_p} parameter is preferred over the model without one, supporting the findings in G. M. Kennedy (2020).
3. Neither model is able to replicate the 4 au width difference, and instead have a 1 au wider apocenter. Future modeling should test whether a Gaussian semi-major axis distribution for the particles as opposed to the uniform one employed here can alleviate this tension.
4. Neither model could reproduce the 21% ± 1% brightness asymmetry near apocenter measured from the radial profile of the data, suggesting there is a yet missing component to the physics underlying the distribution of material in the disk. J. B. Lovell et al. (2025) present a model with an eccentricity gradient that can simultaneously account for the width and brightness difference.
5. We do not detect any emission from the IB discovered in JWST/MIRI imaging, but are able to place a 3σ upper limit of 396 μJy for the total flux at 1.33 mm.
6. We discovered a spectral line in the archival Cycle 3 data centered at $\nu_{\rm obs} \approx 230.25$ GHz at the location of the GDC, redshifted from the expected CO (2–1) line by more than 400 km s^{-1}. This high velocity supports the conclusion that the object is a background galaxy. We suggest that the spectral line could be from CO (3–2) emission at a rest frequency of 345 GHz, implying a redshift of $z \approx 0.502$.

Fomalhaut's proximity allows observations to resolve its structure at higher resolution than other systems, which continues to make it an ideal target to explore the early evolution of planetary systems. These new data reveal variation in the azimuthal structure of the outer disk that is not well-fitted by current eccentric models. Future

observations could provide further insights into the disk's radial substructure on spatial scales, where we could measure its eccentric morphology and test whether it is consistent with the architecture characteristic of sculpting by an internal planet.

Acknowledgments

We acknowledge the contributions of Wayne Holland to the initial ALMA proposal that resulted in this letter. Dr. Holland unfortunately passed away before this work reached its conclusion.

This letter makes use of the following ALMA data: ADS/JAO.ALMA#2013.1.00486.S, #2015.1.00966.S, and #2017.1.01043.S. ALMA is a partnership of ESO (representing its member states), NSF (USA) and NINS (Japan), together with NRC (Canada), MOST and ASIAA (Taiwan), and KASI (Republic of Korea), in cooperation with the Republic of Chile. The Joint ALMA Observatory is operated by ESO, AUI/NRAO and NAOJ. The National Radio Astronomy Observatory is a facility of the National Science Foundation operated under cooperative agreement by Associated Universities, Inc.

This work utilized the Alpine high performance computing resource at the University of Colorado Boulder. Alpine is jointly funded by the University of Colorado Boulder, the University of Colorado Anschutz, Colorado State University, and the National Science Foundation (award 2201538).

This work utilized the Blanca condo computing resource at the University of Colorado Boulder. Blanca is jointly funded by computing users and the University of Colorado Boulder.

M.A.M. acknowledges support for part of this research from the National Aeronautics and Space Administration (NASA) under award number 19-ICAR19_2-0041.

J.B.L. acknowledges the Smithsonian Institute for funding via a Submillimeter Array (SMA) Fellowship.

J.S.C. gratefully acknowledges Kirk Long for optimizing the particle-based models presented in this work.

L.M. acknowledges funding by the European Union through the E-BEANS ERC project (grant No. 100117693). Views and opinions expressed are, however, those of the author(s) only and do not necessarily reflect those of the European Union or the European Research Council Executive Agency. Neither the European Union nor the granting authority can be held responsible for them.

O.P. acknowledges support from the Science and Technology Facilities Council of the United Kingdom, grant No. ST/T000287/1.

A.M.H. gratefully acknowledges support from the National Science Foundation under grant No. ASTR-2307920.

Software: `numpy` (C. R. Harris et al. 2020), `matplotlib` (J. D. Hunter 2007), `CASA` (J. P. McMullin et al. 2007), `uvmodelfit` (I. Martí-Vidal et al. 2014), `astropy`, `regions`, `spectral-cube`, (Astropy Collaboration et al. 2022), `emcee` (D. Foreman-Mackey et al. 2013), `galario` (M. Tazzari et al. 2018), `kepler` (D. Foreman-Mackey et al. 2021), `scipy` (P. Virtanen et al. 2020), `numba` (S. K. Lam et al. 2015).

ORCID iDs

Jay S. Chittidi https://orcid.org/0000-0002-4985-028X
Meredith A. MacGregor https://orcid.org/0000-0001-7891-8143
Joshua Bennett Lovell https://orcid.org/0000-0002-4248-5443
Gaspard Duchene https://orcid.org/0000-0002-5092-6464
Mark Wyatt https://orcid.org/0000-0001-9064-5598
Olja Panic https://orcid.org/0000-0002-6648-2968
Paul Kalas https://orcid.org/0000-0002-6221-5360
A. Meredith Hughes https://orcid.org/0000-0002-4803-6200
David J. Wilner https://orcid.org/0000-0003-1526-7587
Grant M. Kennedy https://orcid.org/0000-0001-6831-7547
Luca Matrà https://orcid.org/0000-0003-4705-3188
Michael P. Fitzgerald https://orcid.org/0000-0002-0176-8973
Kate Y. L. Su https://orcid.org/0000-0002-3532-5580

References

Acke, B., Min, M., Dominik, C., et al. 2012, A&A, 540, A125
Astropy Collaboration, Price-Whelan, A. M., Lim, P. L., et al. 2022, ApJ, 935, 167
Backman, D. E., & Paresce, F. 1993, in Protostars and Planets III, ed. E. H. Levy & J. I. Lunine (Tucson, AZ: Univ. Arizona Press), 1253
Boley, A. C., Payne, M. J., Corder, S., et al. 2012, ApJL, 750, L21
Dermott, S. F., & Murray, C. D. 1980, Icar, 43, 338
Foreman-Mackey, D., Hogg, D. W., Lang, D., & Goodman, J. 2013, PASP, 125, 306
Foreman-Mackey, D., Luger, R., Agol, E., et al. 2021, JOSS, 6, 3285
Gáspár, A., & Rieke, G. 2020, PNAS, 117, 9712
Gáspár, A., Wolff, S. G., Rieke, G. H., et al. 2023, NatAs, 7, 790
Gontcharov, G. A. 2006, AstL, 32, 759
Harris, C. R., Millman, K. J., van der Walt, S. J., et al. 2020, Natur, 585, 357
Holland, W. S., Greaves, J. S., Zuckerman, B., et al. 1998, Natur, 392, 788
Hunter, J. D. 2007, CSE, 9, 90
Kalas, P., Graham, J. R., Chiang, E., et al. 2008, Sci, 322, 1345
Kalas, P., Graham, J. R., & Clampin, M. 2005, Natur, 435, 1067
Kalas, P., Graham, J. R., Fitzgerald, M. P., & Clampin, M. 2013, ApJ, 775, 56
Kass, R. E., & Raftery, A. E. 1995, JASA, 90, 773
Kennedy, G. M. 2020, RSOS, 7, 200063
Kennedy, G. M., Lovell, J. B., Kalas, P., & Fitzgerald, M. P. 2023, MNRAS, 524, 2698
Kenyon, S. J., Currie, T., & Bromley, B. C. 2014, ApJ, 786, 70
Lam, S. K., Pitrou, A., & Seibert, S. 2015, in Proc. Second Workshop on the LLVM Compiler Infrastructure in HPC, LLVM '15 (New York: ACM), 1
Lawler, S. M., Greenstreet, S., & Gladman, B. 2015, ApJL, 802, L20
Lovell, J. B., Lynch, E., Chittidi, J. S., et al. 2025, ApJ, 990, 145
Lovell, J. B., & Lynch, E. M. 2023, MNRAS, 525, L36
Lovell, J. B., Marino, S., Wyatt, M. C., et al. 2021, MNRAS, 506, 1978
Lynch, E. M., & Lovell, J. B. 2022, MNRAS, 510, 2538
MacGregor, M. A., Hurt, S. A., Stark, C. C., et al. 2022, ApJL, 933, L1
MacGregor, M. A., Matrà, L., Kalas, P., et al. 2017, ApJ, 842, 8
MacGregor, M. A., Weinberger, A. J., Hughes, A. M., et al. 2018, ApJ, 869, 75
Mamajek, E. E. 2012, ApJL, 754, L20
Marino, S. 2019, ApJ, 881, 84
Marino, S. 2022, arXiv:2202.03053
Martí-Vidal, I., Vlemmings, W. H. T., Muller, S., & Casey, S. 2014, A&A, 563, A136
Matrà, L., MacGregor, M. A., Kalas, P., et al. 2017, ApJ, 842, 9
McMullin, J. P., Waters, B., Schiebel, D., Young, W., & Golap, K. 2007, in ASP Conf. Ser. 376, Astronomical Data Analysis Software and Systems XVI, ed. R. A. Shaw, F. Hill, & D. J. Bell (San Francisco, CA: ASP), 127
Pan, M., Nesvold, E. R., & Kuchner, M. J. 2016, ApJ, 832, 81
Pearce, T. D., Krivov, A. V., Sefilian, A. A., et al. 2024, MNRAS, 527, 3876
Sepulveda, A. G., Matrà, L., Kennedy, G. M., et al. 2019, ApJ, 881, 84
Sommer, M., Wyatt, M., & Han, Y. 2025, MNRAS, 539, 439
Stapelfeldt, K. R., Holmes, E. K., Chen, C., et al. 2004, ApJS, 154, 458
Tazzari, M., Beaujean, F., & Testi, L. 2018, MNRAS, 476, 4527
van Leeuwen, F. 2007, A&A, 474, 653
Virtanen, P., Gommers, R., Oliphant, T. E., et al. 2020, NatMe, 17, 261
White, J. A., Boley, A. C., Dent, W. R. F., Ford, E. B., & Corder, S. 2017, MNRAS, 466, 4201
Wyatt, M. C., Dermott, S. F., Telesco, C. M., et al. 1999, ApJ, 527, 918
Ygouf, M., Beichman, C. A., Llop-Sayson, J., et al. 2024, AJ, 167, 26